Applied Catalysis B: Environment and Energy 355 (2024) 124156

Contents lists available at ScienceDirect

Applied Catalysis B: Environment and Energy

journal homepage: www.elsevier.com/locate/apcatb

# Vacancy modulation on NiTi-layered double hydroxides towards highly selective $CO_2$ photoreduction

Congjia Luo [a,b,1], Zeyang Li [a,b,1], Yuan Deng [a], Lei Wang [a,b], Enze Xu [a], Jianchi Zhou [a], Xin Zhang [a], Jiong Li [c], Xiaoyu Hu [d], Bin Wang [d], Yibo Dou [a,b,*], Yusen Yang [a,b,*], Min Wei [a,b,*]

[a] State Key Laboratory of Chemical Resource Engineering, Beijing Advanced Innovation Center for Soft Matter Science and Engineering, Beijing University of Chemical Technology, Beijing 100029, PR China
[b] Institute for Innovation in Resource Chemical Engineering, Quzhou, Zhejiang 324000, PR China
[c] Shanghai Synchrotron Radiation Facility, Shanghai Institute of Applied Physics, Chinese Academy of Sciences, Shanghai 201204, PR China
[d] Beijing Research Institute of Chemical Industry, Sinopec Group, Beijing 100013, PR China

ARTICLE INFO

*Keywords:*
*Photocatalytic $CO_2$ conversion*
*Layered double hydroxides*
*Dual active sites*
*Reaction mechanism*

ABSTRACT

Photoreduction of carbon dioxide ($CO_2$) is a promising way to achieve sustainable energy production and alleviate environmental problems. Herein, we report a NiTi-layered double hydroxides photocatalyst with bivalent and trivalent metal vacancies (denoted as $Ni_VTi_V$-LDHs) *via* alkali-etching amphoteric metal cations (Zn and Al) from NiZnTiAl-LDHs precursor. The $Ni_VTi_V$-LDHs attains a $CH_4$ selectivity of 94% with a production rate of 2398 μmol $g^{-1}$ $h^{-1}$, which is preponderant to the state-of-the-art photocatalysts. *Operando* X-ray absorption fine structure (XAFS) and Fourier-transform infrared spectroscopy (FT-IR) characterizations combined with density functional theory (DFT) calculations corroborate that $Ni^{2+\delta}$–O(H)–$Ti^{3+\zeta}$ sites modulated by adjacent vacancies exhibits a declined 3*d*-orbital occupancy, accelerating the charge transfer for boosting $CH_4$ formation. Moreover, the unique adsorption configuration ($Ni^{2+\delta}/Ti^{3+\zeta}$–C≡O) not only stabilizes the key intermediate *CO for further protonation, but also induces a decreased energy barrier of the rate-determining step (hydrogenation of $*OCH_3$), accounting for the robust photocatalytic $CO_2$ reduction towards $CH_4$.

## 1. Introduction

Solar-driven photocatalytic reduction of carbon dioxide ($CO_2$) to high-value-added feedstock represents a sustainable energy technology for synchronously alleviating the greenhouse effect and energy crisis [1–3]. Due to the multiple proton-coupled electron transfer process, photocatalytic $CO_2$ reduction would produce a series of products with a similar reduction potential, such as CO, $CH_3OH$, $CH_4$, and even advanced C2+ hydrocarbons[4,5]. Among these products, $CH_4$ with high energy density, as a principal component in liquefied natural gas, has drawn tremendous attention[6]. Considerable efforts have been devoted to the preparation of photocatalysts for $CO_2$-to-$CH_4$ yield and selectivity, including oxide, sulfide, bismuth oxychloride (BiOX), metal-organic frameworks (MOFs), g-$C_3N_4$ and so on[7–10]. Although $CO_2$ reduction to $CH_4$ with relatively a lower reduction potential is more thermodynamically favorable than other product formation, it suffers from sluggish kinetics owing to the complex eight-electron-transfer process. The intricate transfer paths result in the generation of undesired byproducts, which inhibits the improvement of $CH_4$ selectivity[11,12]. Therefore, it remains a huge challenge to develop highly active photocatalysts to steer the reduction reaction pathway of $CO_2$ towards $CH_4$ formation.

From the viewpoint of kinetics, the sustainable proton and electron input into $CO_2$ is essential for the $CH_4$ formation, which indicates that the photocatalysts should boost the generation of separated charges during the process of $CO_2$ reduction[13]. In this regard, the creation of coordination unsaturated metallic sites is an effective way to meet the above requirement[14–18]. On the one hand, the coordination unsaturated metallic sites with a low occupancy of outermost orbital can act as charge-capturing center, which enhances electron-hole separation and charge transfer towards $CO_2$ and/or intermediates. On the other hand, the coordination unsaturated metallic sites are normally positively

* Corresponding authors at: State Key Laboratory of Chemical Resource Engineering, Beijing Advanced Innovation Center for Soft Matter Science and Engineering, Beijing University of Chemical Technology, Beijing 100029, PR China.
*E-mail addresses:* douyb@buct.edu.cn (Y. Dou), yangyusen@buct.edu.cn (Y. Yang), weimin@buct.edu.cn (M. Wei).
[1] These authors contributed equally.

https://doi.org/10.1016/j.apcatb.2024.124156
Received 4 March 2024; Received in revised form 17 April 2024; Accepted 3 May 2024
Available online 7 May 2024
0926-3373/© 2024 Elsevier B.V. All rights are reserved, including those for text and data mining, AI training, and similar technologies.

charged, which is favorable for promoting the proton transfer and hydrogenation of the key intermediates. Notably, the eight-electron-transfer path would easily bifurcate to form various intermediates and byproducts, even though sufficient separated charges are supplied[19–24]. Especially, the elementary step (*CO protonation to *CHO) is widely regarded as the critical process of $CH_4$ formation, which is severely restrained by the competition against *CO desorption [25,26]. Currently, advanced photocatalysts with dual-metal sites used for photocatalytic $CO_2$ reduction have attracted great attention. Especially, the synergetic effect of dual-metal sites would bond C1 intermediates strongly, which results in the preferential reduction path of $CO_2$ towards $CH_4$ and $C_{2+}$[27,28]. In this case, one can imagine that if *CO intermediate is bonded at dual-metal sites, an enhanced *CO stability would promote the desired pathway (*CO protonation to *CHO). Accordingly, dual-metal sites with low coordination numbers are expected to synergistically modulate the reaction path *via* successive hydrogenation of *CO for the production of exclusive $CH_4$ [29–32].

Inspired by this scenario, we modulated the coordination unsaturated structure of transitional metal sites in layered double hydroxides (LDHs) through a vacancy (V) engineering strategy, so as to boost photocatalytic $CO_2$ reduction towards $CH_4$ (Fig. 1a). As a proof of concept, a $Ni_VTi_V$-LDHs sample rich in metal cation vacancy is prepared *via* alkali-etching amphoteric Zn/Al elements in NiZnTiAl-LDHs precursor. Accordingly, the created vacancy leads to the generation of unsaturated dual metal sites ($Ni^{2+\delta}$–O(H)–$Ti^{3+\zeta}$: $0 < \delta < 1$, $0 < \zeta < 1$), which is identified as the key feature for selective $CO_2$-to-$CH_4$ based on a series of *in-situ* tracking characterizations and theoretical simulations. We demonstrate that the decreased occupancy of *d* orbital in coordination unsaturated $Ni^{2+\delta}O_{5.2}$ and $Ti^{3+\zeta}O_{3.0}$ units promotes electron-hole separation, which supplies abundant charge carriers for boosting the kinetics of eight-electron-involved $CH_4$ formation. In addition, the $Ni^{2+\delta}$–O(H)–$Ti^{3+\zeta}$ dual sites synergistically strengthen the stability of *CO intermediate with a unique bridge adsorption configuration, which facilitates *CO protonation and reduces the energy barrier of the rate-determining step (hydrogenation of *$OCH_3$: 0.42 eV). As a result, the resultant $Ni_VTi_V$-LDHs affords a high $CH_4$ production rate of 2398 μmol $g^{-1}$ $h^{-1}$ with a selectivity of 94%. This work delivers a precise regulation over coordination of metal sites through vacancy engineering, which is instructive for the design of efficient photocatalysts towards $CO_2$ reduction.

## 2. Experimental section

### 2.1. Preparation of catalysts of $Ni_VTi_V$-LDHs

As a precursor, the NiZnTiAl-LDHs sample was synthesized *via* a urea co-precipitation method. Firstly, $Zn(NO_3)_2{\cdot}6\,H_2O$ (0.54 g), $Al(NO_3)_3{\cdot}9\,H_2O$ (0.52 g), $Ni(NO_3)_2{\cdot}6\,H_2O$ (5.24 g) and urea (4.50 g) were dissolved in deionized water (300 mL); then concentrated HCl (97 μL) and $TiCl_4$ (97 μL) were added to the above solution in a water bath at 95

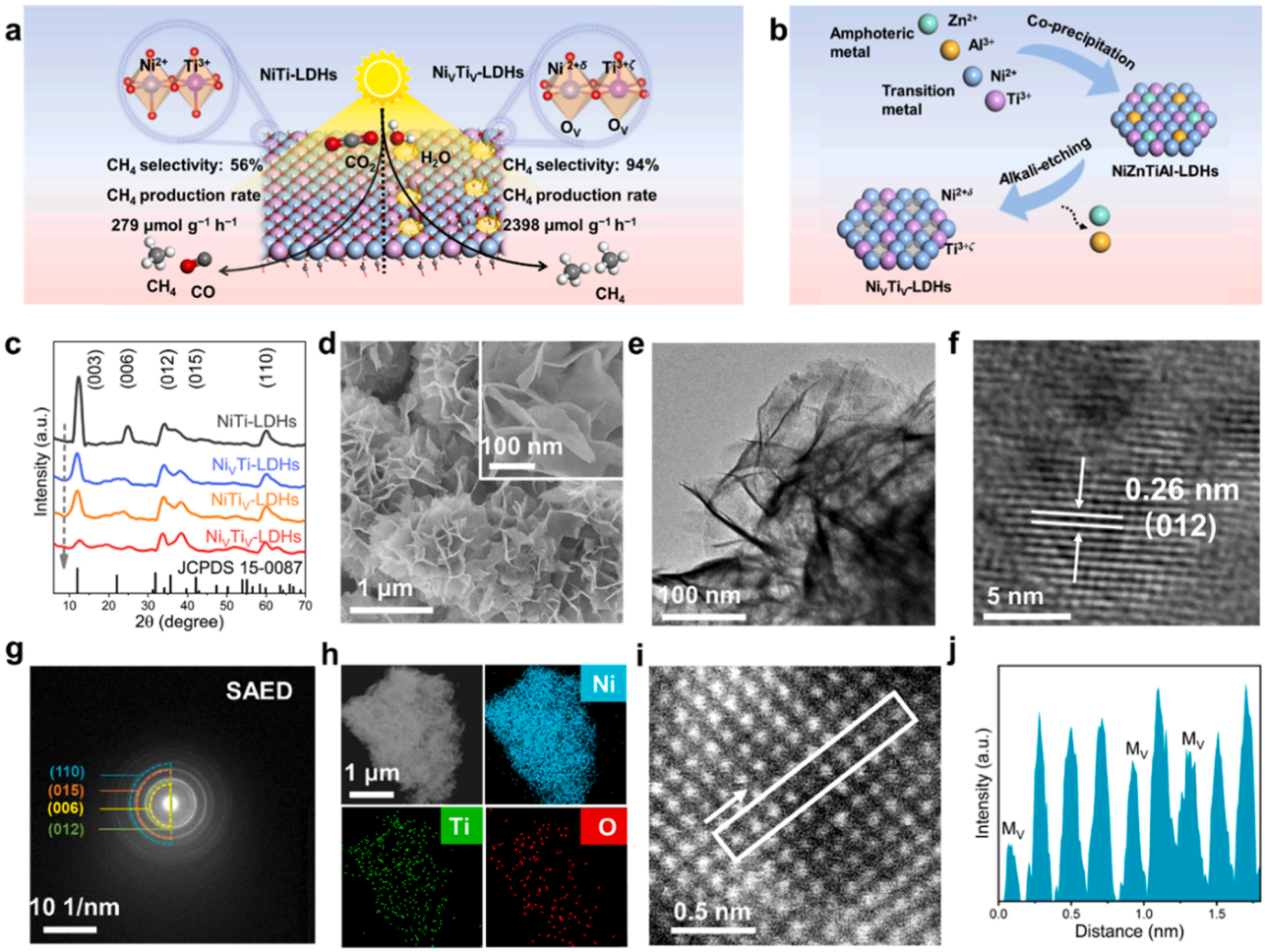


**Fig. 1.** (a) Schematic diagram for the vacancy modulation strategy on $Ni_VTi_V$-LDHs towards photocatalytic $CO_2$ reduction. (b) Schematic illustration for the preparation of $Ni_VTi_V$-LDHs *via* alkali-etching method. (c) XRD patterns of NiTi-LDHs, $Ni_VTi$-LDHs, $NiTi_V$-LDHs and $Ni_VTi_V$-LDHs samples. (d) SEM images, (e) TEM image, (f) HRTEM lattice fringe image, (g) SAED pattern, (h) EDS elemental mapping images, (i) ac-HAADF-STEM image, and (j) corresponding line intensity profile along the selected atom column in (i) for the $Ni_VTi_V$-LDHs sample.

°C for 24 h. The obtained precipitation was centrifugated, washed with water, and dried at 60 °C for 12 h to obtain the NiZnTiAl-LDHs sample. The $Ni_VTi_V$-LDHs sample was synthesized through an alkali-etching method. Typically, the fresh NiZnTiAl-LDHs sample was dispersed in a KOH solution (3 M), stirring vigorously for 3 h. The resulting product was centrifugated, washed thoroughly with water, and dried at 60 °C for 12 h to obtain the $Ni_VTi_V$-LDHs sample. As reference samples, NiZnTi-LDHs, NiTiAl-LDHs and NiTi-LDHs were prepared *via* the above-mentioned urea precipitation method with appropriate chemical composition; and the corresponding $Ni_V$Ti-LDHs and $NiTi_V$-LDHs as control samples were prepared based on a similar alkali-etching method.

### 2.2. Evaluation of photocatalytic performance towards $CO_2$ reduction

The photocatalytic $CO_2$ reduction experiment was conducted in a Teflon-lined stainless reaction chamber with a quartz window at the top for light irradiation. The photocatalyst (30 mg) was installed in the reaction chamber. Prior to the photoreaction, the chamber was evacuated with a mechanical pump. Then, $CO_2$ bubbled through water was introduced and a 300 W Xe lamp (MC-PF300C, Beijing Merry Change Technology Co., Ltd) was employed as the light source. The products at regular intervals from the chamber were analyzed by GC (Shimadzu GC-2014 C) equipped with a TDX-1 column and a thermal conductivity detector (TCD), using He as the carrier gas.

### 2.3. Evaluation of photoelectric chemical properties

The photoelectrochemical measurements were carried out in a three-electrode system under the illumination of 300 W Xe lamp. Ag/AgCl and platinum were used as the reference and counter electrode, respectively. The slurry was prepared by adding 15 mg of the sample, 20 μL of Nafion (5%), and 500 μL of ethyl alcohol to fabricate photoelectrode. The obtained paste is drip-coated on fluorine doped tin oxide (FTO) coated glass with 1 $cm^2$ area to obtain a homogenous film, which was used as working electrode. 0.5 M $Na_2SO_4$ is taken as electrolyte. Mott-Schottky plots were recorded at a frequency of 500, 1000 and 1500 Hz. The photocurrent was recorded by 30 s light on and 30 s light off experiment. The electrochemical impedance spectroscopy (EIS) experiments were recorded at a high frequency of $10^5$ Hz and low frequency of 0.01 Hz.

### 2.4. Operando XAFS measurements

*Operando* X-ray absorption fine structure spectroscopy (XAFS) at the Ni K-edge and Ti K-edge (transmission mode for Ni K-edge and fluorescence mode for Ti K-edge) was carried out at the beamline BL11B of SSRF (Shanghai Synchrotron Radiation Facility), Shanghai Institute of Applied Physics, Chinese Academy of Sciences (CAS). Typically, the photocatalyst sample was poured into the infrared mold and carefully placed into a homemade *in situ* reaction microdevice equipped with polyimide windows. The physically adsorbed impurities were removed by flowing pure He (30 mL $min^{-1}$) before the reaction. Firstly, XAFS spectrum was collected under dark condition. Subsequently, the photocatalyst was illuminated with a xenon lamp and XAFS spectra were collected. Then, a certain amount of $H_2O$ was carefully evaporated into the *operando* cell in $CO_2$ flow (30 mL $min^{-1}$) at 60 °C to trigger the surface reaction and XAFS spectra were collected. All the XAFS data were processed using Athena software package.

## 3. Results and discussion

### 3.1. Fabrication and structural characterizations of $Ni_VTi_V$-LDHs

The schematic illustration for the vacancy modulation on LDHs is presented in Fig. 1**b**. Firstly, NiZnTiAl-LDHs samples composed of transition metal (Ni+Ti) and amphoteric metal (Zn+Al) are obtained *via* a facile co-precipitation method. Then, the Zn/Al elements are removed from LDHs layer through alkali-etching treatment to generate metal vacancy ($V_M$) as well as oxygen vacancy ($V_O$), which induces the coordination unsaturation of the remaining Ni/Ti metal sites. The etched LDHs herein is denoted as $Ni_VTi_V$-LDHs. With a similar strategy, control samples $Ni_V$Ti-LDHs (with Ni vacancy) and $NiTi_V$-LDHs (with Ti vacancy) are obtained through alkali-etching NiZnTi-LDHs and NiTiAl-LDHs, respectively. The X-ray diffraction (XRD) patterns for the various LDHs precursors are shown in Figure S1, which are indexed to a crystalline LDHs phase (JCPDS card no.15–0087). After an alkali-etching treatment, the XRD patterns retain characteristic reflections of LDHs, indicating that the alkali-etching of amphoteric Zn/Al elements would not cause the collapse of the layered structure (Fig. 1**c**). However, the etched LDHs samples exhibit weaker reflections and wider half-peak width than the LDHs precursors, suggesting a defective crystallinity. Inductively coupled plasma atomic emission spectroscopy (ICP-AES) is used to analyze the elemental composition of various samples before and after alkali-etching. The results confirm that Zn and Al elements are almost completely removed from the LDHs laminate (Table S1 and S2). By varying the amphoteric metal proportion (Zn and Al) in NiZnTiAl-LDHs precursors, $Ni_VTi_V$-LDHs samples with tunable $V_M$ concentration of ~7.5%, ~15%, ~22.5%, and ~30% are feasibly obtained.

Scanning electron microscopy (SEM) (Fig. 1**d** and Figure S2) and transmission electron microscopy (TEM) images (Fig. 1**e** and Figure S3a) display that the alkali-etched LDHs samples inherit the nanosheet-like morphology of LDHs precursors. The high-resolution transmission electron microscopy image (HRTEM) shows a clear lattice fringe with an interplanar spacing of ~0.26 nm, which is assigned to the (012) plane of $Ni_VTi_V$-LDHs (Fig. 1**f** and Figure S3b); corresponding selected area electron diffraction (SAED) pattern (Fig. 1**g**) illustrates four diffraction rings indexed to the (110), (015), (006) and (012) plane, respectively. Furthermore, a uniform and homogeneous distribution of Ni, Ti, and O elements in $Ni_VTi_V$-LDHs is distinctly illustrated by energy dispersive spectrometer (EDS) (Fig. 1**h**). In addition, the intensity profile transformed from the aberration-corrected high-angle annular dark-field scanning transmission electron microscopy (ac-HAADF-STEM) image presents a periodic oscillation pattern corresponding to (012) plane of $Ni_VTi_V$-LDHs. Notably, the absence of metal sites is observed along the selected region (in the white frame), indicating the existence of $V_M$ as Zn and Al are removed *via* alkali etching (Fig. 1**i**, **j** and Figure S4).

Raman spectroscopy also validates the presence of $V_M$ for various etched LDHs samples (Fig. 2**a**). Compared with the coordination saturated NiTi-LDHs sample without vacancy, a new band at 658 $cm^{-1}$ assigned to the vibration of −OH group adjacent to $V_M$ is detected for $Ni_VTi_V$-LDHs, and the characteristic bands ascribed to Ni/Ti−O and hydroxyl (O−H) groups after alkali-etching show tiny variation[33,34]. Then, we investigate the influence of vacancy modulation on chemical states of remaining Ni and Ti. As for the saturated NiTi-LDHs, X-ray photoelectron spectroscopy (XPS) displays the $Ni^{2+}$ $2p_{3/2}$ peak at ~855.9 eV. In contrast, the binding energy of $Ni^{2+}$ $2p_{3/2}$ in $Ni_V$Ti-LDHs, $NiTi_V$-LDHs, and $Ni_VTi_V$-LDHs is positively shifted by ~0.1, ~0.3, and ~0.6 eV, respectively (Fig. 2**b**). Similarly, a positive shift of $Ti^{3+}$ $2p_{3/2}$ is also found for these three etched LDHs samples relative to NiTi-LDHs (Fig. 2**c**)[35–37]. The results confirm a modified local electronic density of $Ni^{2+\delta}$ and $Ti^{3+\zeta}$ sites ($0 < \delta < 1$, $0 < \zeta < 1$), since alkali etching induces a decreased metal coordination number in LDHs layer. Meanwhile, the $V_O$ concentration measured by XPS gives the following order: $Ni_VTi_V$-LDHs > $NiTi_V$-LDHs > $Ni_V$Ti-LDHs > NiTi-LDHs (Fig. 2**d**). The comparison study verifies that the alkali-etching process creates both $V_M$ (pushing-electron) and $V_O$ (pulling-electron), which imposes great influence on the electronic structure of Ni and Ti sites.

To deeply uncover the variation of electronic and coordination structure of etched LDHs samples, we performed the X-ray absorption fine structure (XAFS) measurements. As shown in Fig. 2**e**, X-ray absorption near-edge structure (XANES) curves for Ni species show the intensity of white line peak enhances along with the following order:

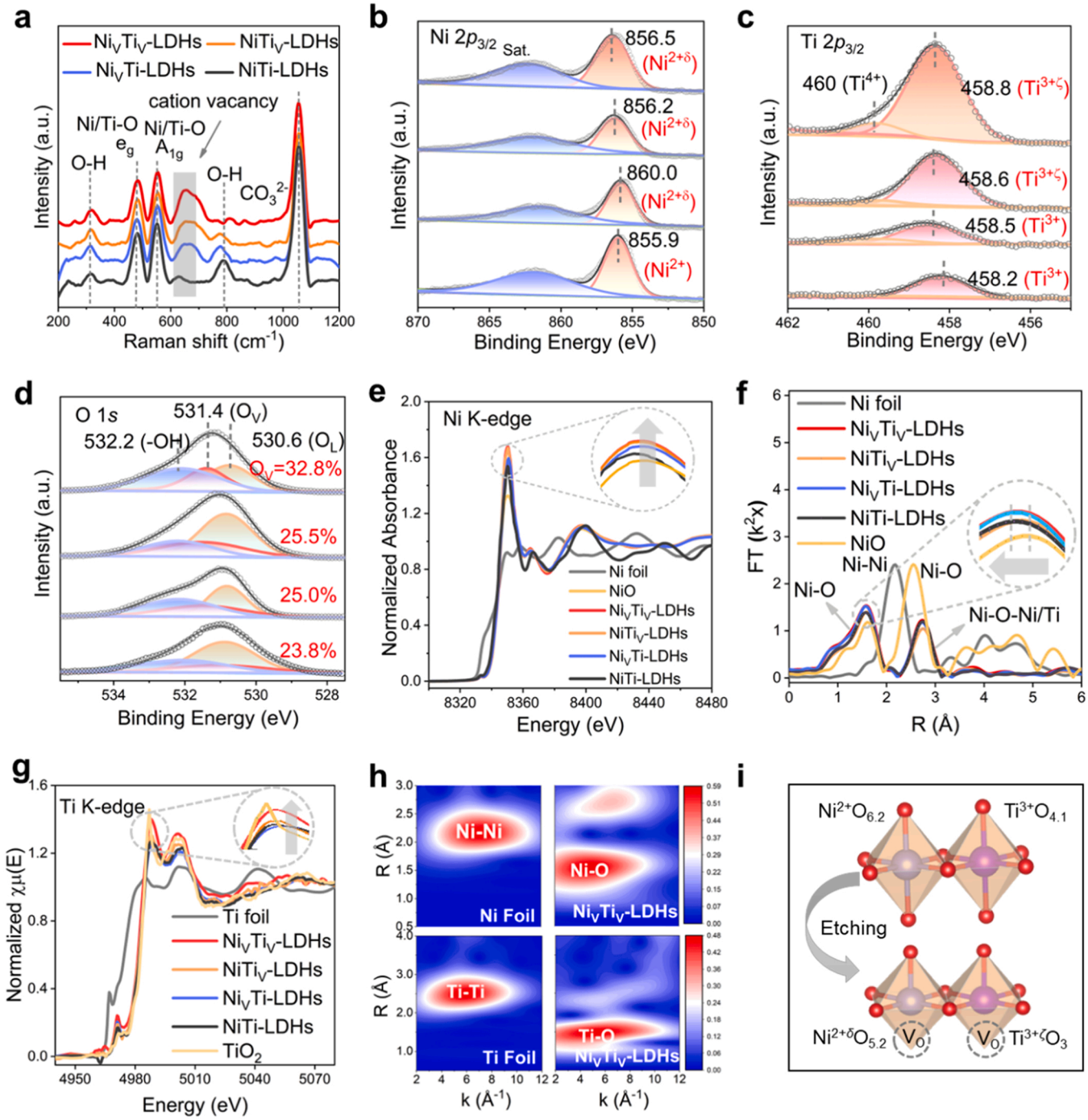


**Fig. 2.** (a) Raman spectra, and high-resolution XPS spectra of (b) Ni $2p_{3/2}$, (c) Ti $2p_{3/2}$ and (d) O 1 *s* for $Ni_VTi_V$-LDHs, $NiTi_V$-LDHs, $Ni_VTi$-LDHs and NiTi-LDHs (from top to bottom in order). (e) Ni K-edge XANES spectra, (f) corresponding $k^2$-weighted FT of EXAFS spectra, (g) Ti K-edge XANES spectra, (h) Wavelet transforms for $k^2$-weighted EXAFS signals at Ni K-edge and Ti K-edge for various samples. (i) Schematic diagram of metal coordination structure for NiTi-LDHs (top) and $Ni_VTi_V$-LDHs (bottom).

NiO < NiTi-LDHs < $Ni_VTi$-LDHs < $NiTi_V$-LDHs < $Ni_VTi_V$-LDHs (Fig. 2**e**; inset), indicating an increase in the Ni valence state in turn ($Ni^{2+\delta}$, $0 < \delta < 1$). Compared with NiTi-LDHs, the extended X-ray absorption fine structure (EXAFS) spectra show a reduction of the K-edge oscillations (0–12 Å) for the $Ni_VTi_V$-LDHs, indicating the variations of the coordination environment of Ni sites after alkali-etching (Figure S5a). The corresponding *R*-space spectra display two representative peaks at 1.56 and 2.75 Å, which are ascribed to the first shell Ni−O bond and the second shell Ni−O−Ni/Ni−O−Ti coordination, respectively (Fig. 2**f**) [38–42]. The average distance of the first shell Ni−O bond in $Ni_VTi_V$-LDHs is 1.56 Å, which is shorter than that of control sample NiO (1.62 Å). Analogously, Ti K-edge XANES spectra (Fig. 2**g**) show the $Ni_VTi_V$-LDHs sample gives the strongest absorption edge intensity among all these LDHs samples, indicating the existence of $Ti^{3+\zeta}$ site ($0 < \zeta < 1$)[43]. The results confirm that the vacancy modulation *via* alkali-etching on NiTi-LDHs leads to the variation of Ni and Ti electronic structure (Fig. 2**h, S5b−d** and **S6**). In addition, K-edge EXAFS fitting graph and data (Table S3, S4 and Figure S7−**S10**) verify a 5.2-coordination ($Ni^{2+\delta}O_{5.2}$) and 3.0-coordination ($Ti^{3+\zeta}O_{3.0}$) structure for the $Ni_VTi_V$-LDHs sample, much lower than NiTi-LDHs with the 6.2-coordination

($NiO_{6.2}$) and 4.1-coordination ($TiO_{4.1}$) structure (Fig. 2**i**). The results above demonstrate that $V_M$ creation is feasible for modulating the coordination and electronic structure of metal sites on LDHs.

### 3.2. Evaluation on photocatalytic $CO_2$ reduction performance

The photocatalytic performance of various LDHs samples towards $CO_2$ reduction reaction was investigated by using a gas-solid reaction under full light irradiation, without adding sacrificial reagents or photosensitizers. As shown in Fig. 3**a** and **b**, the $Ni_VTi_V$-LDHs sample exhibits the highest production rate of $CH_4$ (2398 μmol $g^{-1}$ $h^{-1}$), which is ~8.6 times larger than that of NiTi-LDHs; moreover, an ultrahigh selectivity of 94% towards $CH_4$ in the presence of $Ni_VTi_V$-LDHs is obtained (Fig. 3**c**). Notably, an incremental trend of $CH_4$ production rate is observed for $Ni_VTi_V$-LDHs as the $V_M$ concentration enhances from 7.5% to 15%, and then remains almost constant along with further increase. In contrast, the $CH_4$ selectivity displays a volcanic curve within 7.5−30% (Fig. 3**d**). Based on a comprehensive consideration, the $Ni_VTi_V$-LDHs with $V_M$ concentration of 15% is thus chosen as the optimized photocatalyst. In addition, the product $O_2$ of the $H_2O$ oxidation as half reaction was investigated. As shown in Figure S11, the production rate of $O_2$ on $Ni_VTi_V$-LDHs and NiTi-LDHs is 4660 μmol $g^{-1}$ $h^{-1}$ and 544 μmol $g^{-1}$ $h^{-1}$, respectively. We summarized the recently reported advanced photocatalysts for $CO_2$ reduction to $CH_4$ (Table S5), and the results show

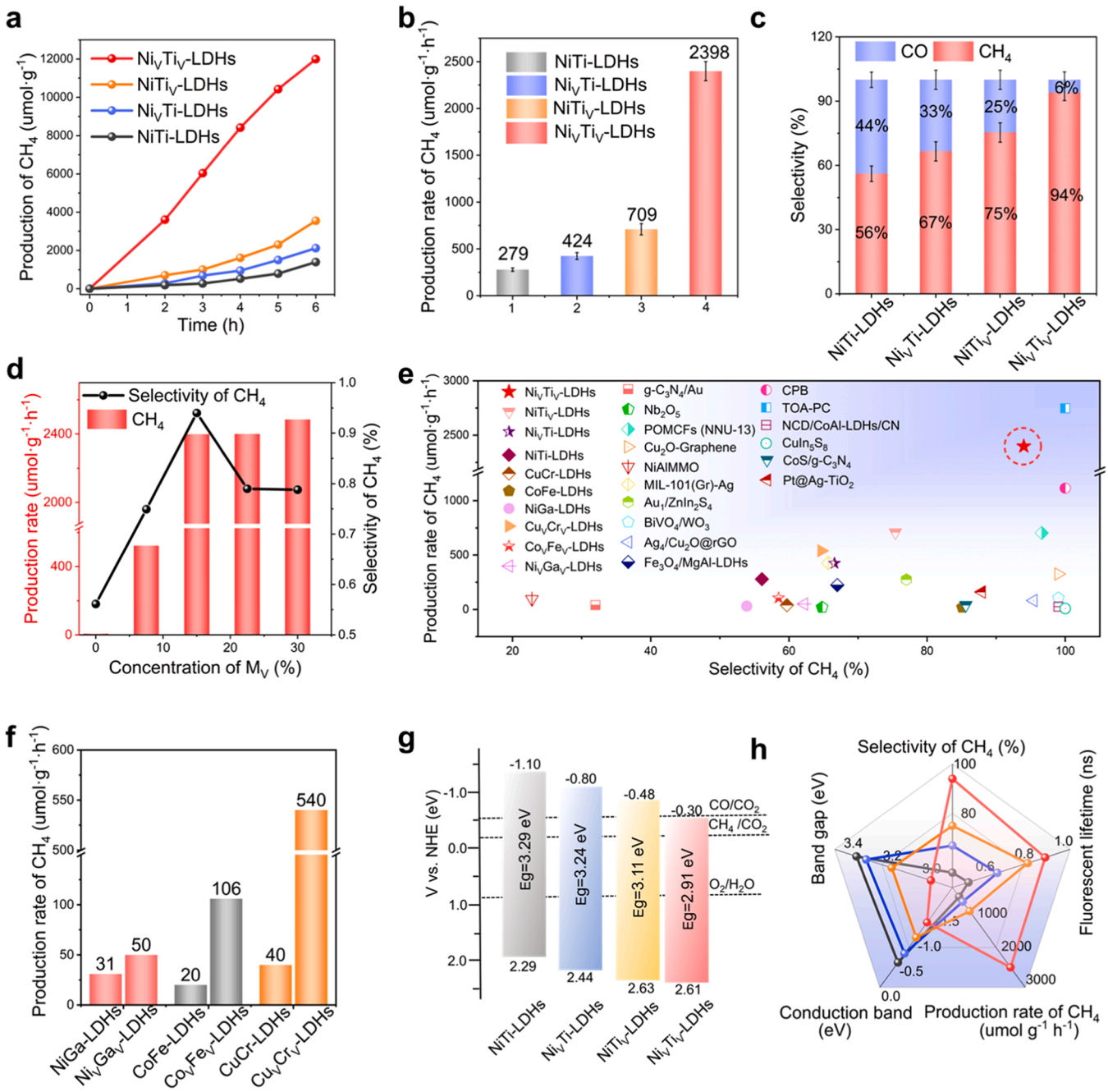


**Fig. 3.** (a) $CH_4$ production as a function of reaction time. (b) Production rate and (c) selectivity of $CH_4$ for $Ni_VTi_V$-LDHs, $NiTi_V$-LDHs, $Ni_VTi$-LDHs and NiTi-LDHs. (d) Influence of $V_M$ concentration on $CO_2$ photoreduction performance. (e) Comparison of photocatalytic $CO_2$-to-$CH_4$ performance between $Ni_VTi_V$-LDHs in this work and previously reported photocatalysts. (f) $CH_4$ production rate for various saturated LDHs and corresponding defective LDHs obtained *via* alkali-etching method. (g) Schematic diagram of band structure. (h) Comprehensive performance comparison for $Ni_VTi_V$-LDHs, $NiTi_V$-LDHs, $Ni_VTi$-LDHs and NiTi-LDHs.

the optimized $Ni_VTi_V$-LDHs sample with a $CH_4$ production rate of 2398 μmol $g^{-1}$ $h^{-1}$ and a selectivity of 94% is preponderant to the state-of-the-art photocatalysts (Fig. 3**e**).

Then, a series of control experiments were conducted (Figure S12). No detectable products are found when the experiments are carried out in dark, or in $N_2$, or without photocatalyst or $H_2O$, which confirms the product is only obtained through $CO_2$ reduction in the presence of $Ni_VTi_V$-LDHs upon light irradiation. In addition, no significant decrease in activity is observed after five cycles of testing (Figure S13). The used $Ni_VTi_V$-LDHs sample maintains its original crystal structure and morphology as displayed in XRD pattern and SEM image (Figure S14), which verifies a satisfactory photocatalytic stability. In addition, several other LDHs samples with $V_M$ including $Ni_VGa_V$-LDHs, $Co_VFe_V$-LDHs and $Cu_VCr_V$-LDHs were also prepared *via* alkali-etching LDHs precursors (Figure S15). As shown in Fig. 3**f**, a similar enhanced photocatalytic performance of these defective LDHs is achieved, demonstrating that the vacancy modulation strategy can be extended to other LDHs materials towards photocatalytic $CO_2$ reduction to $CH_4$.

### 3.3. Investigations on the mechanism of photocatalytic $CO_2$ reduction

To elucidate the underlying reasons for the improved $CO_2$ photoreduction performance, we then investigated the specific reaction processes, primarily including light harvesting, electron-hole separation and $CO_2$ reduction by photoexcited electrons. Since the first and second steps are closely associated with the intrinsic properties of photocatalysts, the photoelectric properties of various NiTi-LDHs are systemically characterized[44–46]. Firstly, the $Ni_VTi_V$-LDHs displays an enhanced UV–vis diffuse reflection spectrum (UV–vis DRS) absorption in the range 200−800 nm relative to NiTi-LDHs (Figure S16a). The band gap ($E_g$) values of $Ni_VTi_V$-LDHs, $NiTi_V$-LDHs, $Ni_VTi$-LDHs and NiTi-LDHs are 2.91, 3.11, 3.24 and 3.29 eV, respectively, obtained from the Tauc diagram of UV–vis DRS (Figure S16b). Meanwhile, the flat band energies ($E_{FB}$) calculated from the Mott–Schottky characterization are −0.40, −0.58, −0.90 and −1.20 eV (*vs* Ag/AgCl electrode), respectively (Figure S17). Correspondingly, valence band energies ($E_{VB}$) are 2.61, 2.63, 2.44 and 2.29 eV (*vs* normal hydrogen electrode (NHE)),

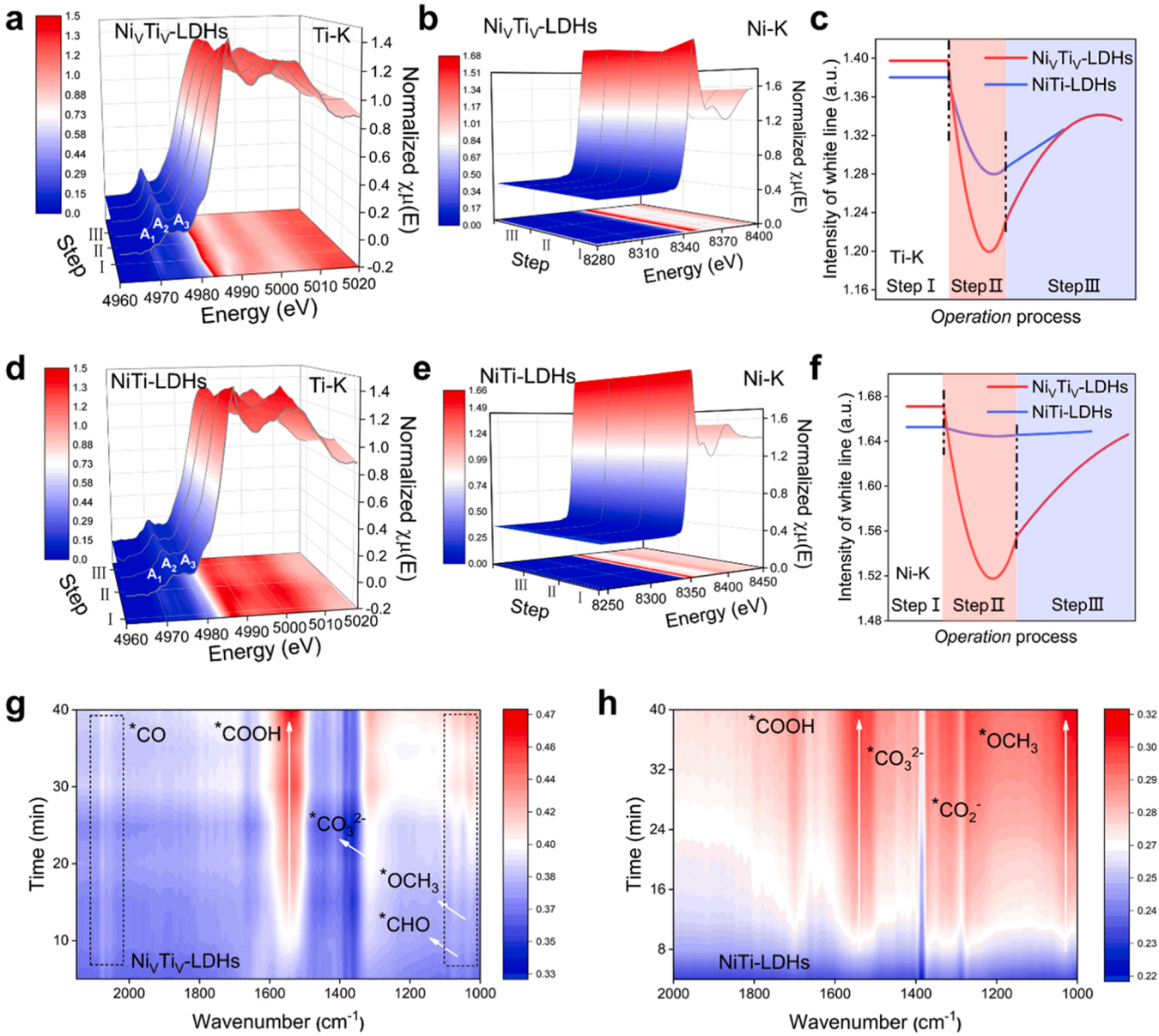


**Fig. 4.** *Operando* XANES spectra of (a) Ti and (b) Ni K-edge for $Ni_VTi_V$-LDHs. (c) Comparison of normalized white line strength of Ti K edge between $Ni_VTi_V$-LDHs and NiTi-LDHs. *Operando* XANES spectra of (d) Ti and (e) Ni K-edge for NiTi-LDHs. (f) Comparison of normalized white line strength of Ni K edge between $Ni_VTi_V$-LDHs and NiTi-LDHs. *Operando* FT-IR spectra for (g) $Ni_VTi_V$-LDHs and (h) NiTi-LDHs in the presence of $CO_2$ and $H_2O$ vapor under light irradiation.

respectively (Fig. 3**g**)[47,48]. The results confirm that the unsaturated $Ni^{2+\delta}$ and $Ti^{3+\zeta}$ sites result in a regulation on the band structure of $Ni_VTi_V$-LDHs. Notably, the conduction band energy ($E_{CB}$) of $Ni_VTi_V$-LDHs is located between the reduction potential of CO and $CH_4$, which improves the $CH_4$ selectivity. In contrast, the $E_{CB}$ of $NiTi_V$-LDHs, $Ni_VTi$-LDHs and NiTi-LDHs is higher than the reduction potential of CO, leading to a relatively poor $CH_4$ selectivity (Fig. 3**d**).

In addition, the lifetime of photogenerated electrons is prolonged from 0.48 ns for NiTi-LDHs to 0.87 ns for $Ni_VTi_V$-LDHs (Figure S18 and Table S6), illustrating a significantly improved electron-hole separation efficiency after vacancy modulation. Moreover, the $Ni_VTi_V$-LDHs manifests the lowest photoluminescence spectroscopy (PL) peak intensity, the lowest interfacial resistance and the highest photocurrent density among these LDHs samples (Figure S19), indicating both boosted electron-hole separation and carrier transfer. Finally, electron paramagnetic resonance (EPR) is conducted to detect the spin-active $\bullet O^{2-}$ and $\bullet OH^-$ species by using 5,5-dimethyl-1-pyrroline N-oxide (DMPO) as the spin trapping agent under light irradiation (Figure S20). The $Ni_VTi_V$-LDHs sample exhibits the strongest EPR signals, accounting for the best surficial redox activity towards $CH_4$ production (2398 μmol $g^{-1}$ $h^{-1}$). In summary, the $Ni_VTi_V$-LDHs takes the advantages of light harvesting, electron-hole separation and surficial redox activity, in comparison with other LDHs samples (Fig. 3**h**), which significantly promotes photocatalytic $CO_2$ reduction to $CH_4$.

Subsequently, the transport dynamics of photogenerated electrons on photocatalysts was investigated through *operando* XAFS characterizations. When the measurement condition is varied from darkness to light irradiation, the white line intensity of Ti (Fig. 4**a**) and Ni (Fig. 4**b**) K edge for $Ni_VTi_V$-LDHs declines significantly, indicating a decrease in the Ni and Ti valence state owing to electron transfer to surface metal sites (electron accumulation at $Ni^{2+\delta}$ and $Ti^{3+\zeta}$ sites). Then, both $CO_2$ and $H_2O$ are introduced into the reaction cell, and the white line intensity of Ti and Ni K edge increases gradually along with reaction time, as a result of the charge transfer from $Ni_VTi_V$-LDHs surface to substrate $CO_2$. This phenomenon is also found in the sample of NiTi-LDHs (Fig. 4**d** and **e**), but the magnitude of the change is rather small (Fig. 4**c** and **f**). The results above corroborate that the more positively charged $Ni^{2+\delta}$ and $Ti^{3+\zeta}$ sites as trapping sites are conducive to the accumulation and transfer of photoexcited electrons, which hence provides a kinetically feasible process for $CO_2$ reduction.

In addition, *operando* Fourier-transform infrared spectroscopy (FT-IR) is used to study the adsorbed species and reaction intermediates. Primarily, $CO_2$ and $H_2O$ vapor are introduced into the reaction cell to explore $CO_2$ adsorption process on $Ni_VTi_V$-LDHs under dark condition for 10 min (Figure S21). The characteristic bands of $CO_2^-$ at 1670 and 1288 $cm^{-1}$, bicarbonate ($HCO_3^-$) at 1647 $cm^{-1}$, monodentate carbonate (m-$CO_3^{2-}$) at 1464 $cm^{-1}$ and bidentate carbonate (b-$CO_3^{2-}$) at 1373 $cm^{-1}$ are clearly observed[49,50]. Combined with the *operando* XANES results above, this indicates the adsorption of $CO_2$ molecule at the unsaturated $Ni^{2+\delta}$–O(H)–$Ti^{3+\zeta}$ dual sites on the photocatalyst surface. Then, the characteristic vibration peaks are recorded to evaluate the occurrence of surface reaction under light irradiation (from 0 to 40 min) (Fig. 4**g**). The band intensities of both asymmetric and symmetric $\nu_{O-C-O}$ (1361 and 1384 $cm^{-1}$) of $CO_3^{2-}$ decline progressively, illustrating a gradual consumption of adsorbed $CO_3^{2-}$ during the photocatalytic reaction. Meanwhile, the characteristic bands at 2076/2058 $cm^{-1}$ and 1541 $cm^{-1}$ ascribed to bridge adsorption of *CO and *COOH species are observed, whose intensity enhances gradually under light irradiation. This indicates the activation and transformation of $CO_2$ to *COOH and then to *CO intermediate on $Ni_VTi_V$-LDHs. Most importantly, new characteristic peaks at 1030/1026 $cm^{-1}$ and 1067 $cm^{-1}$ appear, which are ascribed to the two intermediates (*CHO and *$OCH_3$) during $CO_2$ reduction to $CH_4$[51,52]. In contrast, for the sample of saturated NiTi-LDHs, the signal of $CO_2$ adsorption is extremely weak in dark. Upon light irradiation, the characteristic band of *COOH with a weak intensity is found at 1541 $cm^{-1}$ whilst *CO is not detected (Fig. 4**h**). The results substantiate that *CO intermediate prefers to binding with the $Ni^{2+\delta}$–O(H)–$Ti^{3+\zeta}$ dual sites on $Ni_VTi_V$-LDHs surface, which then experiences hydrogenation to produce *CHO and *$OCH_3$ intermediates, accounting for the high selectivity towards $CH_4$. In addition, *operando* XPS spectroscopy shows the concentration of $V_O$ for $Ni_VTi_V$-LDHs decreases from 32.2% to 29.6% when the gaseous $H_2O$ is introduced into the reaction cell (Figure S22). The results indicate that $H_2O$ molecule tends to be adsorbed at the $V_O$ for subsequent oxidation, which is consistent with previously reported results[53,54].

The density functional theory calculations of spin-polarized Hubbard correction (DFT + $U$) were carried out to disclose the role of $Ni^{2+\delta}$–O(H)–$Ti^{3+\zeta}$ sites for promoted $CO_2$ photoreduction performance, and the $Ni_VTi_V$-LDHs and NiTi-LDHs model systems were built (Figure S23). The $Ni_VTi_V$-LDHs displays an obvious shift of $Ni^{2+\delta}$ $d_{xy}/d_{z^2}$ orbital and $Ti^{3+\zeta}$ $d_{xy}/d_{yz}/d_{xz}$orbital towards the Fermi level (Fig. 5**a** and **b**); and its $d$ band center (−1.75 eV) moves upward relative to NiTi-LDHs (−1.98 eV), owing to the presence of unsaturated $Ni^{2+\delta}$–O(H)–$Ti^{3+\zeta}$ sites (Fig. 5**c**). This induces the location of antibonding states above the Fermi level, which results in a less filling of antibonding states and thereby facilitates charge transfer to the lowest unoccupied molecular orbital (LUMO) of $CO_2$[55–58]. Moreover, $CO_2$ molecule experiences physical adsorption on the surface of $Ni_VTi_V$-LDHs with Ni–O–C–O–Ti configuration (Figure S24a). In contrast, the optimized results show that $CO_2$ molecule undergoes a bridge adsorption configuration (Ni–C–O–Ti) on $Ni_VTi_V$-LDHs (Figure S24b), which is also reported in previous work[45,47]. This agrees well with the results of *operando* FT-IR monitored b-$CO_3^{2-}$ adsorption (Figure S21). The corresponding PDOS shows an efficient hybridization of Ni/Ti 3$d$ and $CO_2$ $s/p$ orbital (Fig. 5**d**). In addition, the differential charge (Fig. 5**e**) and Bader charge analysis (Figure S25) ascertain a more obvious charge accumulation and transfer to absorbed $CO_2$ on $Ni_VTi_V$-LDHs (1.05 eV) than that on NiTi-LDHs (0.63 eV). Furthermore, both Ni $d_{yz}$ and Ti $d_{xz}$ in $Ni_VTi_V$-LDHs are closer to the Fermi level, indicating a more efficient charge transfer from these two orbitals to $CO_2$ (Fig. 5**f** and **g**). The results corroborate that the $Ni^{2+\delta}$ and $Ti^{3+\zeta}$ sites with declined 3$d$-orbital occupancy serve as trapping center, which accelerates electron transfer to $CO_2$ molecule and boosts the kinetics of multiple-electron-involved $CH_4$ production.

In addition, the Gibbs free energy calculations on the catalytic reaction of $CO_2$-to-$CH_4$ were conducted, in combination with *operando* experimental characterizations to give an in-depth understanding on reaction pathway (Fig. 5**h** and **i**). In the case of $Ni_VTi_V$-LDHs, firstly, $CO_2$ activation proceeds *via* the binding of O and C atoms at the $Ni^{2+\delta}$–O(H)–$Ti^{3+\zeta}$ dual sites. After accepting electrons from the catalyst surface, the *$CO_2$ converts to carboxyl radical (*COOH) (step I), followed by *COOH dehydration to key intermediate *CO (step II). The Ni/Ti $d$-band center moves towards the Fermi level (Ni $d_{yz}$ by 0.49 eV, Ti $d_{xz}$ by 0.73 eV) with *CO adsorption, indicating the strong stabilization of *CO (Fig. 5**f** and **g**). This is well identified by *operando* FT-IR characterizations, in which $Ni_VTi_V$-LDHs strengthens the *CO adsorption *via* the unique $Ni^{2+\delta}(Ti^{3+\zeta})$–C≡O configuration. Accordingly, the $Ni_VTi_V$-LDHs exhibits a larger ΔΔG value (energy barrier difference between *CO to *CHO and *CO to CO (g)) (0.62 eV) relative to NiTi-LDHs, which facilitates the formation of *CHO intermediate (step III) rather than CO desorption. Subsequently, *CHO experiences successive hydrogenation steps to $CH_4$ (five-electron-involved): step IV: →$OCH_2$, step V: →*$OCH_3$, step VI: →*$OHCH_3$, step VII: →*$CH_3$, step VIII: →*$CH_4$. Finally, $CH_4$ desorbs from the catalyst surface *via* a spontaneous exothermic process. It should be noted that the conversion of *$OCH_3$ to *$OHCH_3$ (step VI) gives the largest energy barrier (0.69 eV), which is confirmed as the rate-determining step. For the NiTi-LDHs system, a similar reaction pathway is also found. However, the NiTi-LDHs displays a higher energy barrier (1.11 eV) of rate-determining step (*$OCH_3$ to *$OHCH_3$) for $CH_4$ production whilst a less ΔΔG value (0.39 eV) for competition again *CO desorption, which results in the relatively poor $CH_4$ production and selectivity. Therefore, the $Ni^{2+\delta}$–O(H)–$Ti^{3+\zeta}$ dual-sites on $Ni_VTi_V$-LDHs

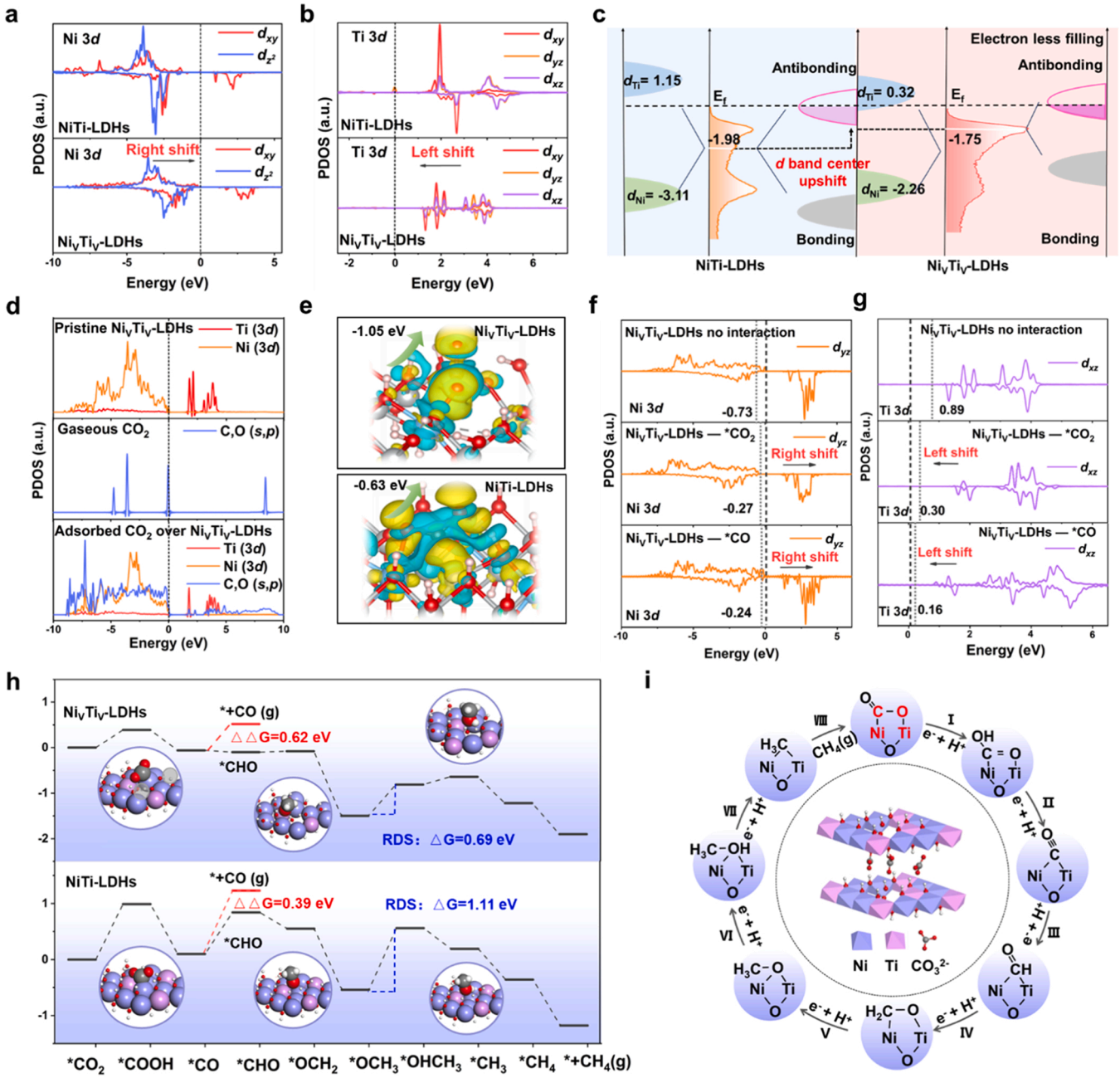


**Fig. 5.** PDOS of (a) Ni 3*d* (*xy* and $z^2$) and (b) Ti 3*d* (*xy*, *yz*, and *xz*) for NiTi-LDHs and Ni$_V$Ti$_V$-LDHs. (c) *d*-band structure diagram of NiTi-LDHs and Ni$_V$Ti$_V$-LDHs based on *d*-orbital coupling engineering ($E_f$ represents the Fermi level.). (d) PDOS for Ni$_V$Ti$_V$-LDHs, gaseous $CO_2$ and adsorbed $CO_2$ on Ni$_V$Ti$_V$-LDHs. (e) Charge difference plots for $CO_2$ adsorbed on Ni$_V$Ti$_V$-LDHs (up) and NiTi-LDHs (down). PDOS of (f) Ni 3$d_{yz}$ and (g) Ti 3$d_{xz}$orbital for *$CO_2$ and *CO adsorbed on Ni$_V$Ti$_V$-LDHs. (h) Reaction free-energy profiles of photocatalytic $CO_2$-to-$CH_4$ over Ni$_V$Ti$_V$-LDHs (up) and NiTi-LDHs (down). The insets display the adsorption of *$CO_2$, *$OCH_3$ and *$OHCH_3$ intermediates on corresponding photocatalyst. (i) Reaction mechanism of photocatalytic $CO_2$-to-$CH_4$ on the surface of Ni$_V$Ti$_V$-LDHs.

not only stabilize the *CO key intermediate, but also decrease the energy barrier of rate-determining step (*$OCH_3$ to *$OHCH_3$), accounting for the largely boosted $CH_4$ production.

## 4. Conclusions

In summary, a Ni$_V$Ti$_V$-LDHs photocatalyst is obtained by tuning coordination unsaturated $Ni^{2+\delta}$–O(H)–$Ti^{3+\zeta}$ sites *via* an alkali-etching strategy, which displays an excellent performance for photocatalytic $CO_2$-to-$CH_4$ conversion. The conjunction of *operando* experimental characterizations and theoretical calculations enables a deep corroboration on the vacancy modification towards robust $CO_2$ photoreduction. The Ni$_V$Ti$_V$-LDHs displays a key feature of unsaturated $Ni^{2+\delta}$–O(H)–$Ti^{3+\zeta}$ dual-sites with a decreased *d*-orbital occupancy, which strengthens the generation and transfer of photoexcited electron. Accordingly, a strong affinity of key intermediate (*CO) *via* a unique $Ni^{2+\delta}(Ti^{3+\zeta})$–C≡O configuration is achieved, favorable for the subsequent hydrogenation towards the production of $CH_4$. Moreover, the unsaturated dual-sites lower the energy barrier of rate-determining step (*$OCH_3$ to *$OHCH_3$), which accelerates the multielectron transfer process in $CO_2$-to-$CH_4$. As a result, the synergistic $Ni^{2+\delta}$–O(H)–$Ti^{3+\zeta}$ dual-sites exhibits a high $CH_4$ production rate and selectivity. This work provides a strategy for regulating the coordination/electronic structure of materials based on defect engineering, which can be extended to the design of other

photocatalysts towards efficient solar energy conversion.

## CRediT authorship contribution statement

**Yuan Deng:** Software, Methodology, Investigation. **Min Wei:** Writing – review & editing, Conceptualization. **Zeyang Li:** Writing – original draft, Visualization, Software, Formal analysis. **Yusen Yang:** Writing – review & editing, Validation, Supervision, Project administration. **Congjia Luo:** Writing – original draft, Investigation, Formal analysis. **Yibo Dou:** Writing – review & editing, Validation, Supervision, Conceptualization. **Jianchi Zhou:** Validation, Methodology. **Enze Xu:** Software, Formal analysis. **Lei Wang:** Software, Methodology, Formal analysis, Conceptualization. **Bin Wang:** Validation, Software, Project administration. **Xiaoyu Hu:** Validation, Resources. **Jiong Li:** Validation, Resources, Methodology. **Xin Zhang:** Supervision, Project administration.

## Declaration of Competing Interest

The authors declare that they have no known competing financial interests or personal relationships that could have appeared to influence the work reported in this paper.

## Data Availability

Data will be made available on request.

## Acknowledgements

This work was supported by the National Key R&D Program of China (2021YFC2103500), National Natural Science Foundation of China (22278029, 22172006, 22102006 and 22288102), and the Fundamental Research Funds for the Central Universities of China (buctrc202203). The authors are thankful for the support of the Shanghai Synchrotron Radiation Facility during the XAFS measurements at the beamline of BL11B..

## Appendix A. Supporting information

Supplementary data associated with this article can be found in the online version at doi:10.1016/j.apcatb.2024.124156.

## References

[1] Z. Liu, Z. Deng, S. Davis, P. Ciais, Monitoring global carbon emissions in 2022, Nat. Rev. Earth Environ. 4 (2023) 205–206.
[2] G. Ozin, Accelerated optochemical engineering solutions to $CO_2$ photocatalysis for a sustainable future, Matter 5 (2022) 2594–2614.
[3] G. Ozin, What will it take to decarbonize the chemicals and petrochemicals industries with light? Matter 6 (2023) 3688–3690.
[4] R. Ham, C.J. Nielsen, S. Pullen, J.N.H. Reek, Supramolecular coordination cages for artificial photosynthesis and synthetic photocatalysis, Chem. Rev. 123 (2023) 5225–5261.
[5] R. Li, D. Wang, Superiority of dual-atom catalysts in electrocatalysis: one step further than single-atom catalysts, Adv. Energy Mater. 12 (2022) 2103564.
[6] M. Cai, Z. Wu, Z. Li, L. Wang, W. Sun, A.A. Tountas, C. Li, S. Wang, K. Feng, A. B. Xu, S. Tang, A. Tavasoli, M. Peng, W. Liu, A.S. Helmy, L. He, G.A. Ozin, X. Zhang, Greenhouse-inspired supra-photothermal $CO_2$ catalysis, Nat. Energy 6 (2021) 807–814.
[7] J. Li, L. Zhu, C.H. Tung, L.Z. Wu, Engineering graphdiyne for solar photocatalysis, Angew. Chem. Int. Ed. 62 (2023) e202301384.
[8] S. Wu, C. He, L. Wang, J. Zhang, High-efficiency electron tandem flow mode on carbon nitride/titanium dioxide heterojunction for visible light nitrogen photofixation, Chem. Eng. J. 443 (2022) 136425.
[9] R. Yang, Y. Fan, Y. Zhang, L. Mei, R. Zhu, J. Qin, J. Hu, Z. Chen, Y. Hau Ng, D. Voiry, S. Li, Q. Lu, Q. Wang, J.C. Yu, Z. Zeng, 2D transition metal dichalcogenides for photocatalysis, Angew. Chem. Int. Ed. 62 (2023) e202218016.
[10] H. Yin, Z. Zhang, T. Lu, Ordered integration and heterogenization of catalysts and photosensitizers in metal-/covalent-organic frameworks for boosting $CO_2$ photoreduction, Acc. Chem. Res. 56 (2023) 2676–2687.
[11] E. Gong, S. Ali, C.B. Hiragond, H.S. Kim, N.S. Powar, D. Kim, H. Kim, S.-I. In, Solar fuels: research and development strategies to accelerate photocatalytic $CO_2$ conversion into hydrocarbon fuels, Energy Environ. Sci. 15 (2022) 880–937.
[12] D. Zhong, Y. Gong, C. Zhang, T. Lu, Dinuclear metal synergistic catalysis for energy conversion, Chem. Soc. Rev. 52 (2023) 3170–3214.
[13] G. Ren, M. Shi, Z. Li, Z. Zhang, X. Meng, Electronic metal-support interaction via defective-induced platinum modified BiOBr for photocatalytic $N_2$ fixation, Appl. Catal. B: Environ. 327 (2023) 122462.
[14] W. Jiang, H. Loh, B.Q.L. Low, H. Zhu, J. Low, J.Z.X. Heng, K.Y. Tang, Z. Li, X. J. Loh, E. Ye, Y. Xiong, Role of oxygen vacancy in metal oxides for photocatalytic $CO_2$ reduction, Appl. Catal. B: Environ. 321 (2023) 122079.
[15] S. Liang, L. Huang, Y. Gao, Q. Wang, B. Liu, Electrochemical reduction of $CO_2$ to CO over transition metal/N-doped carbon catalysts: the active sites and reaction mechanism, Adv. Sci. 8 (2021) 2102886.
[16] Y. Liu, Y. Zhou, X. Zhou, X. Jin, B. Li, J. Liu, G. Chen, Cu doped $SnS_2$ nanostructure induced sulfur vacancy towards boosted photocatalytic hydrogen evolution, Chem. Eng. J. 407 (2021) 127180.
[17] M. Ni, Y. Zhu, C. Guo, D.-L. Chen, J. Ning, Y. Zhong, Y. Hu, Efficient visible-light-driven $CO_2$ methanation with self-regenerated oxygen vacancies in $Co_3O_4/NiCo_2O_4$ hetero-nanocages: Vacancy-mediated selective photocatalysis, ACS Catal. 13 (2023) 2502–2512.
[18] Z. Zhao, Z. Wang, J. Zhang, C. Shao, K. Dai, K. Fan, C. Liang, Interfacial chemical bond and oxygen vacancy-enhanced $In_2O_3$/CdSe-DETA S-scheme heterojunction for photocatalytic $CO_2$ conversion, Adv. Funct. Mater. 33 (2023) 2214470.
[19] Y. Cao, L. Guo, M. Dan, D.E. Doronkin, C. Han, Z. Rao, Y. Liu, J. Meng, Z. Huang, K. Zheng, P. Chen, F. Dong, Y. Zhou, Modulating electron density of vacancy site by single Au atom for effective $CO_2$ photoreduction, Nat. Commun. 12 (2021) 1675.
[20] L. Liu, Z. Wang, J. Zhang, O. Ruzimuradov, K. Dai, J. Low, Tunable interfacial charge transfer in a 2D–2D composite for efficient visible-light-driven $CO_2$ conversion, Adv. Mater. 35 (2023) 2300643.
[21] H. Ma, X. Wang, T. Tan, X. Zhou, F. Dong, Y. Sun, Stabilize the oxygen vacancies in $Bi_2SiO_5$ for durable photocatalysis via altering local electronic structure with phosphate dopant, Appl. Catal. B: Environ. 319 (2022) 121911.
[22] H. Rao, L.C. Schmidt, J. Bonin, M. Robert, Visible-light-driven methane formation from $CO_2$ with a molecular iron catalyst, Nature 548 (2017) 74–77.
[23] Y. Zhang, J. Zhao, H. Wang, B. Xiao, W. Zhang, X. Zhao, T. Lv, M. Thangamuthu, J. Zhang, Y. Guo, J. Ma, L. Lin, J. Tang, R. Huang, Q. Liu, Single-atom Cu anchored catalysts for photocatalytic renewable $H_2$ production with a quantum efficiency of 56%, Nat. Commun. 13 (2022) 58.
[24] J. Zhou, J. Li, L. Kan, L. Zhang, Q. Huang, Y. Yan, Y. Chen, J. Liu, S. Li, Y. Lan, Linking oxidative and reductive clusters to prepare crystalline porous catalysts for photocatalytic $CO_2$ reduction with $H_2O$, Nat. Commun. 13 (2022) 4681.
[25] Y. Bo, H. Wang, Y. Lin, T. Yang, R. Ye, Y. Li, C. Hu, P. Du, Y. Hu, Z. Liu, R. Long, C. Gao, B. Ye, L. Song, X. Wu, Y. Xiong, Altering hydrogenation pathways in photocatalytic nitrogen fixation by tuning local electronic structure of oxygen vacancy with dopant, Angew. Chem. Int. Ed. 60 (2021) 16085–16092.
[26] Y. Zhang, X. Zhi, J.R. Harmer, H. Xu, K. Davey, J. Ran, S.Z. Qiao, Facet-specific active surface regulation of BixMOy (M=Mo, V, W) nanosheets for boosted photocatalytic $CO_2$ reduction, Angew. Chem. Int. Ed. 61 (2022) e202212355.
[27] S. Deng, R. Wang, X. Feng, R. Zheng, S. Gong, X. Chen, Y. Shangguan, L. Deng, H. Tang, H. Dai, L. Duan, C. Liu, Y. Pan, H. Chen, Dual Lewis acid-base sites regulate silver-copper bimetallic oxide nanowires for highly selective photoreduction of carbon dioxide to methane, Angew. Chem. Int. Ed. 62 (2023) e202309625.
[28] H. Shi, H. Wang, Y. Zhou, J. Li, P. Zhai, X. Li, G.G. Gurzadyan, J. Hou, H. Yang, X. Guo, Atomically dispersed indium-copper dual-metal active sites promoting C−C coupling for CO2 photoreduction to ethanol, Angew. Chem. Int. Ed. 61 (2022) e202208904.
[29] J. Feng, R. Tang, G. Liu, T. Meng, Regulating *d*-orbital electronic character and HER free energy of VN electrocatalyst by anchoring single atom, Chem. Eng. J. 452 (2023) 139131.
[30] Z. Li, C. Mao, Q. Pei, P.N. Duchesne, T. He, M. Xia, J. Wang, L. Wang, R. Song, F. M. Ali, D.M. Meira, Q. Ge, K.K. Ghuman, L. He, X. Zhang, G.A. Ozin, Engineered disorder in $CO_2$ photocatalysis, Nat. Commun. 13 (2022) 7205.
[31] G. Qian, W. Lyu, X. Zhao, J. Zhou, R. Fang, F. Wang, Y. Li, Efficient photoreduction of diluted $CO_2$ to tunable syngas by Ni-Co dual sites through *d*-band center manipulation, Angew. Chem. Int. Ed. 61 (2022) e202210576.
[32] B. Wang, S.Z. Yang, H. Chen, Q. Gao, Y.X. Weng, W. Zhu, G. Liu, Y. Zhang, Y. Ye, H. Zhu, H. Li, J. Xia, Revealing the role of oxygen vacancies in bimetallic $PbBiO_2Br$ atomic layers for boosting photocatalytic $CO_2$ conversion, Appl. Catal. B: Environ. 277 (2020) 119170.
[33] X. Han, B. Lu, X. Huang, C. Liu, S. Chen, J. Chen, Z. Zeng, S. Deng, J. Wang, Novel p- and n-type S-scheme heterojunction photocatalyst for boosted $CO_2$ photoreduction activity, Appl. Catal. B: Environ. 316 (2022) 121587.
[34] E. Musella, I. Gualandi, E. Scavetta, A. Rivalta, E. Venuti, M. Christian, V. Morandi, A. Mullaliu, M. Giorgetti, D. Tonelli, Newly developed electrochemical synthesis of Co-based layered double hydroxides: toward noble metal-free electro-catalysis, J. Mater. Chem. A 7 (2019) 11241–11249.
[35] Q. Wen, K. Yang, D. Huang, G. Cheng, X. Ai, Y. Liu, J. Fang, H. Li, L. Yu, T. Zhai, Schottky heterojunction nanosheet array achieving high-current-density oxygen evolution for industrial water splitting electrolyzers, Adv. Energy Mater. 11 (2021).
[36] Y. Yang, L. Dang, M.J. Shearer, H. Sheng, W. Li, J. Chen, P. Xiao, Y. Zhang, R. J. Hamers, S. Jin, Highly active trimetallic NiFeCr layered double hydroxide electrocatalysts for oxygen evolution reaction, Adv. Energy Mater. 8 (2018) 1703189.

[37] K. Zhu, Q. Zhu, M. Jiang, Y. Zhang, Z. Shao, Z. Geng, X. Wang, H. Zeng, X. Wu, W. Zhang, K. Huang, S. Feng, Modulating Ti $t_{2g}$ orbital occupancy in a Cu/$TiO_2$ composite for selective photocatalytic $CO_2$ reduction to CO, Angew. Chem. Int. Ed. 61 (2022) e202207600.
[38] C. Chen, L. Tao, S. Du, W. Chen, Y. Wang, Y. Zou, S. Wang, Advanced exfoliation strategies for layered double hydroxides and applications in energy conversion and storage, Adv. Funct. Mater. 30 (2020) 1909832.
[39] J. Fan, Y. Zhao, H. Du, L. Zheng, M. Gao, D. Li, J. Feng, Light-induced structural dynamic evolution of Pt single atoms for highly efficient photocatalytic $CO_2$ reduction, ACS Appl. Mater. Interfaces 14 (2022) 26752–26765.
[40] Y. Zhao, Y. Zhao, G.I.N. Waterhouse, L. Zheng, X. Cao, F. Teng, L. Wu, C. Tung, D. O'Hare, T. Zhang, Layered-double-hydroxide nanosheets as efficient visible-light-driven photocatalysts for dinitrogen fixation, Adv. Mater. 29 (2017) 1703828.
[41] J.R. Huang, X.F. Qiu, Z.H. Zhao, H.L. Zhu, Y.C. Liu, W. Shi, P.Q. Liao, X.M. Chen, Single-product faradaic efficiency for electrocatalytic of $CO_2$ to CO at current density larger than 1.2 A $cm^{-2}$ in neutral aqueous solution by a single-atom nanozyme, Angew. Chem. Int. Ed. 61 (2022) e202210985.
[42] X. Wang, S. Xi, P. Huang, Y. Du, H. Zhong, Q. Wang, A. Borgna, Y.W. Zhang, Z. Wang, H. Wang, Z.G. Yu, W.S.V. Lee, J. Xue, Pivotal role of reversible $NiO_6$ geometric conversion in oxygen evolution, Nature 611 (2022) 702–708.
[43] M. Xu, S. He, H. Chen, G. Cui, L. Zheng, B. Wang, M. Wei, $TiO_{2-x}$-modified Ni nanocatalyst with tunable metal–support interaction for water–gas shift reaction, ACS Catal. 7 (2017) 7600–7609.
[44] I. Khan, S. Khan, S.Y. Wu, H.T. Chen, A. Zada, L. Linlin, A. Ismail, S. Ali, F. Raziq, M. Haider, J. Khan, S. Ullah, Sp Ju, S. Wang, Synergistic functionality of dopants and defects in Co-phthalocyanine/B-CN Z-scheme photocatalysts for promoting photocatalytic $CO_2$ reduction reactions, Small 19 (2023) 2208179.
[45] X. Li, Y. Sun, J. Xu, Y. Shao, J. Wu, X. Xu, Y. Pan, H. Ju, J. Zhu, Y. Xie, Selective visible-light-driven photocatalytic $CO_2$ reduction to $CH_4$ mediated by atomically thin $CuIn_5S_8$ layers, Nat. Energy 4 (2019) 690–699.
[46] D. Saito, Y. Tamaki, O. Ishitani, Photocatalysis of $CO_2$ reduction by a Ru(II)–Ru(II) supramolecular catalyst adsorbed on $Al_2O_3$, ACS Catal. 13 (2023) 4376–4383.
[47] J. Li, H. Huang, W. Xue, K. Sun, X. Song, C. Wu, L. Nie, Y. Li, C. Liu, Y. Pan, H.-L. Jiang, D. Mei, C. Zhong, Self-adaptive dual-metal-site pairs in metal-organic frameworks for selective $CO_2$ photoreduction to $CH_4$, Nat. Catal. 4 (2021) 719–729.
[48] J. Wu, Y. Huang, W. Ye, Y. Li, $CO_2$ reduction: from the electrochemical to photochemical approach, Adv. Sci. 4 (2017) 1700194.
[49] K. Sun, Y. Qian, H. Jiang, Metal-organic frameworks for photocatalytic water splitting and $CO_2$ reduction, Angew. Chem. Int. Ed. 62 (2023) e202217565.
[50] R. Wang, Z. Wang, S. Wan, Q. Liu, J. Ding, Q. Zhong, Facile layer regulation strategy of layered double hydroxide nanosheets for artificial photosynthesis and mechanism insight, Chem. Eng. J. 434 (2022) 134434.
[51] L. Cheng, X. Yue, J. Fan, Q. Xiang, Site-specific electron-driving observations of $CO_2$-to-$CH_4$ photoreduction on Co-doped $CeO_2$/crystalline carbon nitride S-scheme heterojunctions, Adv. Mater. 34 (2022) 2200929.
[52] S. Si, H. Shou, Y. Mao, X. Bao, G. Zhai, K. Song, Z. Wang, P. Wang, Y. Liu, Z. Zheng, Y. Dai, L. Song, B. Huang, H. Cheng, Low-coordination single Au atoms on ultrathin $ZnIn_2S_4$ nanosheets for selective photocatalytic $CO_2$ reduction towards $CH_4$, Angew. Chem. Int. Ed. 61 (2022) e202209446.
[53] G. Wan, L. Yin, X. Chen, X. Xu, J. Huang, C. Zhen, H. Zhu, B. Huang, W. Hu, Z. Ren, H. Tian, L. Wang, G. Liu, H. Cheng, Photocatalytic overall water splitting over $PbTiO_3$ modulated by oxygen vacancy and ferroelectric polarization, J. Am. Chem. Soc. 144 (2022) 20342–20350.
[54] R. Shen, Y. Liu, H. Wen, X. Wu, G. Han, X. Yue, S. Mehdi, T. Liu, H. Cao, E. Liang, B. Li, Engineering bimodal oxygen vacancies and Pt to boost the activity toward water dissociation, Small 18 (2022) 2105588.
[55] P. Li, J. Bi, J. Liu, Y. Wang, X. Kang, X. Sun, J. Zhang, Z. Liu, Q. Zhu, B. Han, *p–d* orbital hybridization induced by p-block metal-doped Cu promotes the formation of C2+ products in ampere-level $CO_2$ electroreduction, J. Am. Chem. Soc. 145 (2023) 4675–4682.
[56] X. Sun, L. Sun, G. Li, Y. Tuo, C. Ye, J. Yang, J. Low, X. Yu, J.H. Bitter, Y. Lei, D. Wang, Y. Li, Phosphorus tailors the *d*-Band center of copper atomic sites for efficient $CO_2$ photoreduction under visible-light irradiation, Angew. Chem. Int. Ed. 61 (2022) e202207677.
[57] X. Wang, J. Wang, P. Wang, L. Li, X. Zhang, D. Sun, Y. Li, Y. Tang, Y. Wang, G. Fu, Engineering 3*d*–2*p*–4*f* gradient orbital coupling to enhance electrocatalytic oxygen reduction, Adv. Mater. 34 (2022) 2206540.
[58] X. Yue, L. Cheng, F. Li, J. Fan, Q. Xiang, Highly strained Bi-MOF on bismuth oxyhalide support with tailored intermediate adsorption/desorption capability for robust $CO_2$ photoreduction, Angew. Chem. Int. Ed. 61 (2022) e202208414.